Twin Satellite Orbital and Doppler Parameters for Global Topographic Mapping

Antonio Moccia, Sergio Vetrella, and Marco D'Errico

Università degli Studi di Napoli "Federico II"
Dipartimento di Scienza e Ingegneria dello Spazio
P.le Tecchio 80
80125 Napoli, Italy
Tél. : +39-81-7682158 – Fax : +39-81-7682160
E-mail amoccia @ ds.unina.it

ABSTRACT

The Global Topography Mission (GTM) is a joint USA/Italy project to design and develop a new space system aimed at high resolution topographic mapping of Earth continents and ice caps. This paper presents the results of a numerical simulation of the GTM interferometric SAR system, consisting of two antennae, operating simultaneously, on-board twin satellites flying in parallel orbits. In particular, the orbital and Doppler parameters are analysed, in order to perform a preliminary mission design. The orbital studies are mainly devoted to evaluate the baseline components, including the safety distance between the satellites, and the swath overlap between the two SARs. Whereas, the computed Doppler parameters are successfully compared to analytical expressions existing in literature, the analysis shows that a yaw attitude angle steering which reduces atmospheric drag on solar panels and antennae, determines zero Doppler centroid frequency at boresight and has a positive effect on swath overlap. The conducted analysis puts in evidence the variation of these parameters along the orbit and gives satisfactory results with regard to the interferometric application.

INTRODUCTION

The NASA Topographic Science Working Group (1988) and the Joint Topsat NASA/ASI Working Group (1994) have pointed out the usefulness of high resolution digital elevation models (30 m horizontal resolution, 10 m horizontal accuracy, 1-3 m vertical accuracy) for many scientific applications and, on the other hand, the lack of adequate topographic data over large regions of the Earth and the need for reliable updating procedures of existing maps.

Spaceborne Synthetic Aperture Radar (SAR) interferometry has been successfully applied to obtain digital elevation models (DEMs) (Gabriel and Goldstein, 1988; Prati *et al.*, 1992). In particular, it has the great advantage of night and day, all weather observations with respect to optical remote sensing techniques.

The past and existing space missions (SEASAT, SIR-B, ERS-1) achieve SAR Interferometry by using two images of the same area obtained from cross-track separated orbits (repeat-track interferometry). In this case, the two images forming the interferogram are acquired at different times, which cause a major limitation: time decorrelation (Zebker and Villasenor, 1992). Moreover, a single satellite interferometric mission must take into account differences in propagation delay effects. Other limiting factors are the baseline indetermination, which causes errors in the DEM generation, and the baseline variation, which determines the difficulty of having a satisfactory baseline during the whole mission (Li and Goldstein, 1990; Rodriguez and Martin, 1992; Hagberg and Ulander, 1993). Error analysis of the ERS-1 data showed that they can offer satisfactory results only over selected test sites (Moccia *et al.*, 1994a; Zebker *et al.*, 1994). Although SAR Interferometry is basically a low cost ERS-1 by-product and an improvement in coverage and accuracy might be obtained by ERS-1 and ERS-2 synergism, it must be pointed out that none of the existing space missions can really obtain global coverage with satisfactory height accuracy. On the other hand, the height accuracy depends on the required map scale, which varies in different regions for different applications. As an example the US Geological Survey Vertical Map Accuracy Standards are 3.5 m and 8.5 m for 1:24.000 and 1:100.000 DEM scales, respectively. Therefore, ERS data can be used when the interferometric pair exhibits a satisfactory coherence.

Due to the above reasons, in the last few years JPL (Jet Propulsion Laboratory), NASA GSFC (Goddard Space Flight Center), Alenia Spazio, and University of Naples (under NASA contract in USA and ASI contract in Italy) have been studying a new space mission: the Global Topography Mission (GTM).

The GTM proposed configuration consists of twin satellites flying in formation (D'Errico *et al.*, 1994; Salazar and Kakuda, 1994), each carrying a laser altimeter (Bufton, 1989; Gardner, 1992) and an L-band SAR (one of the two satellites transmitting and both receiving). The twin satellites have the same orbit altitude and inclination, whereas the ascending nodes are slightly displaced to achieve the horizontal baseline, so that the satellites fly on nearly parallel orbits. Thanks to this configuration, the two SAR images forming the interferogram are acquired simultaneously so that temporal decorrelation is avoided. In addition, baseline indetermination is overcome by accurately positioning both antennae thanks to differential GPS (Global Positioning System) (Yunck *et al.*, 1985; Bertiger *et al.*, 1989).

In the last few years the authors developed a computer code for spaceborne SAR simulation (Moccia *et al.*, 1994b) which has now been extended to the analysis of two contemporaneously flying satellites. It accounts for keplerian or perturbated orbit, attitude control and manoeuvres, SAR pointing geometry and radiometric characteristics, Earth ellipsoid, terrain morphology, and surface backscattering characteristics.

In this paper the authors describe the results of the GTM simulation conducted to analyse the Doppler parameters (frequency and bandwidth) and the orbital and interferometric parameters (swath overlap, baseline components, null spacing). This simulation was conducted within the preliminary studies concerning the GTM mission design and performance evaluation.

1. GTM OVERVIEW

GTM will guarantee global coverage by SAR interferometry and regional coverage by laser altimetry. Thanks to both the interferometric SAR and laser altimeter data sets, it will be possible to validate and integrate the SAR and laser DEMs. In order to reduce data rate, during the first part of the mission the SAR will work in the ascending phases while the laser altimeter in the descending ones, vice versa in the second part of the mission. A reduction of shadowing effects will be obtained by integrating the ascending and the descending phase SAR DEMs (Digital Elevation Models). In addition to these GTM features, the authors demonstrated the potentiality of a range steerable antenna for GTM, to provide high temporal resolution for natural disaster applications (D'Errico *et al.*, 1995; D'Errico *et al.*, 1994).

The main goals of GTM can be summarised as follows (Joint TOPSAT NASA/ASI Working Group, 1994):

1. Global elevation measurements with horizontal resolution of 30 m, horizontal accuracy of 10 m, and vertical accuracy of 1-3 m over 90% of Earth land and ice sheets.

2. Regional elevation, roughness, and vegetation height measurements with horizontal resolution of 30 m, horizontal accuracy of 10 m, and vertical accuracy of 20 cm-1 m over selected areas of Earth lands and ice sheets.

3. Complete global coverage in less then 6 months and continue measurements for at least 12 months in order to monitor seasonal and short period changes of ice, vegetation, wetland, and time-varying landforms.

4. Frequent observations in selected local areas during volcanic eruptions, floods, landslides and other natural disasters.

The proposed USA/Italy joint program schedules the GTM ready to launch in the 1998-2000 time frame, thus providing accurate topographic data in a timely manner for EOS (Earth Observing System). The GTM flight configuration is shown in figure 1. The three components of the baseline between the two satellites are defined with respect to an orbiting right-handed reference frame fixed to the transmitting/receiving satellite (origin in the centre of mass, x-axis directed along the velocity vector, y-axis perpendicular to the orbital plane). The interferometric baseline is given by the B_y component while the B_x component is a safety distance, necessary for navigation and to avoid the satellite collision near the poles, where the two orbits intercept. For the sake of completeness, in figure 1 the baseline vertical component (B_z) is also shown, although it is of centimetric order as it will be demonstrated later. The ascending node values of B_x and B_y are listed in table 1.

Of course, the two orbits are identical as far as the unperturbed altitude is concerned, in order to avoid divergence of baseline components and differences in orbit decay. The chosen sun-synchronous altitude and inclination (Table 1)

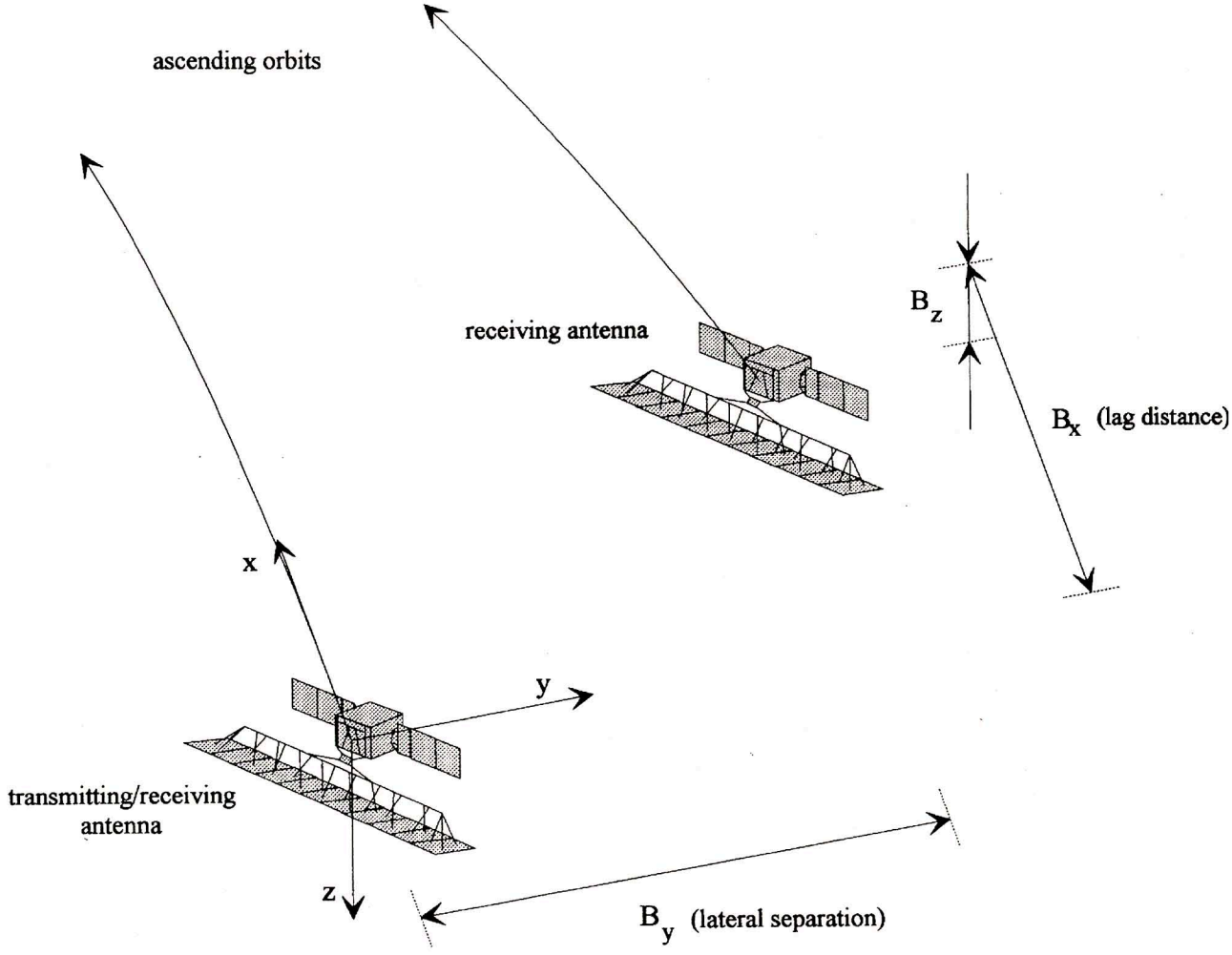

Figure 1 - Position of the receiving satellite with respect to an orbiting reference frame (xyz) fixed to the transmitting/receiving satellite ($B_x>0$, $B_y>0$, $B_z>0$).

Table 1 - Nominal orbital and radar parameters of GTM twin satellites

Orbital Parameters	
altitude (Km)	579.67
sun-synchronous inclination (°)	97.714
equatorial lag distance (m)	265
equatorial lateral separation (m)	2020
Radar Parameters	
off-nadir angle (°)	30
3dB antenna azimuth angle (°)	1.34
3dB antenna elevation angle (°)	3.46
PRF (Hz)	1944.4
wavelenght (cm)	24.0
ground range resolution (m)	30

maximise the observation frequency when a range steerable antenna is adopted (D'Errico *et al.*, 1994).

As shown in figure 2, the twin antennae are left looking in order to increase Antarctica coverage. The selected equatorial lateral separation will not allow SAR interferometry near the poles, therefore in an extended phase of the mission a larger node separation will be carried out. The main radar and antenna parameters are also listed in table 1.

2. YAW ATTITUDE ANGLE STEERING

The twin satellites will adopt yaw attitude angle (γ) steering in order to align the solar panels and the antenna along the spacecraft-atmosphere relative velocity vector ($\underline{V}_a$), so that the atmospheric drag is significantly reduced (figure 2).

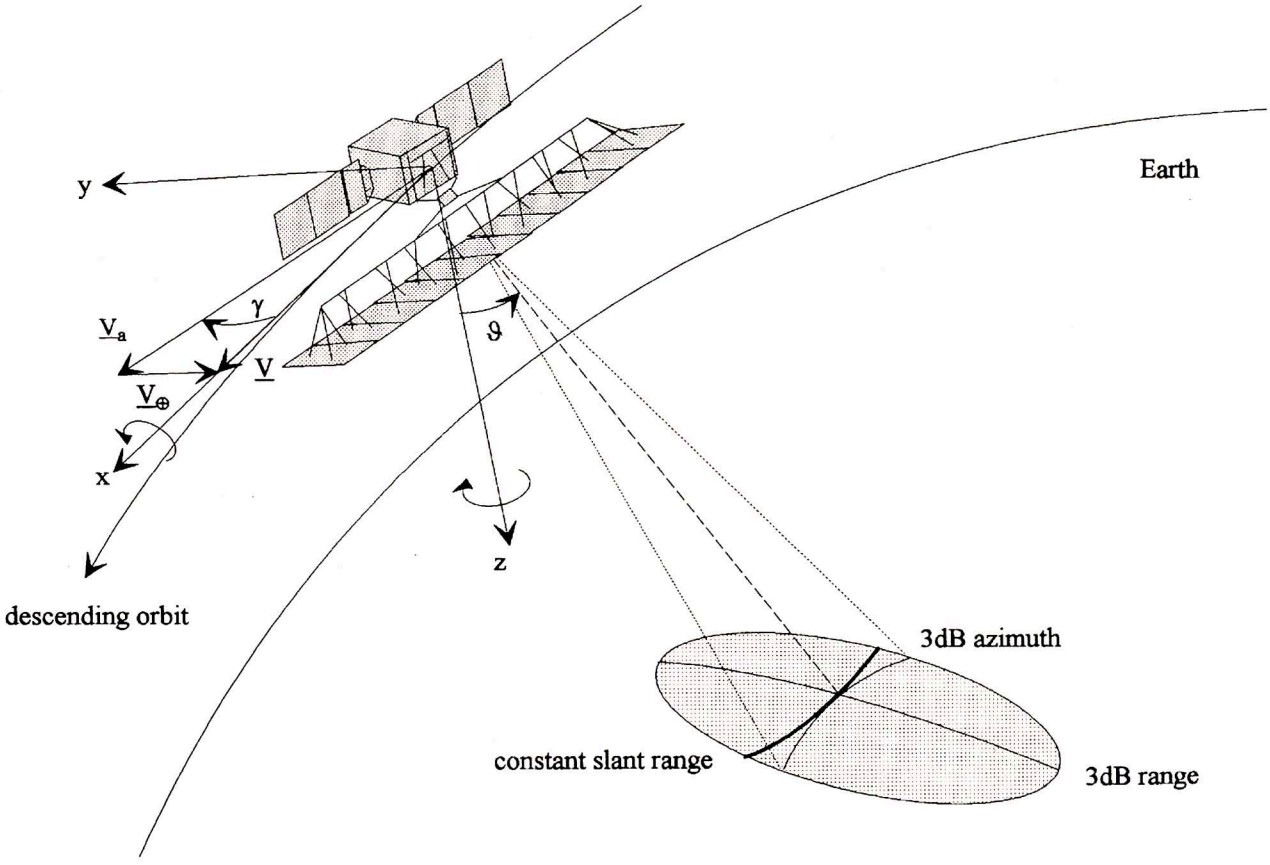

Figure 2 - Viewing geometry of the yaw-steered satellite for atmospheric drag reduction.

The yaw angle can be computed considering the atmosphere fixed to the Earth, as follows:

$$\gamma = \cos^{-1}\left[\frac{(\underline{V} - \underline{V}_\oplus)\cdot \underline{V}}{|\underline{V} - \underline{V}_\oplus||\underline{V}|}\right] \quad (1)$$

where $\underline{V}_\oplus$ is the atmosphere velocity, $\underline{V}$ is the spacecraft velocity. Of course, the velocity vectors are computed as a function of time by the simulation program.

In the case of circular orbit we get:

$$\gamma = \tan^{-1}\left(\frac{\sin i \cos\beta}{\omega/\omega_\oplus - \cos i}\right) \quad (2)$$

being i the constant orbit plane inclination, ω the spacecraft constant angular velocity, and $\omega_\oplus$ the Earth angular velocity. β is the mean anomaly, that is the geocentric angle between the ascending node and the instantaneous satellite position, computed in the orbit plane and positive counterclockwise with respect to the angular momentum (Bate *et al.*, 1971).

Raney (1986) introduced the yaw attitude angle steering to produce zero Doppler centroid frequency in circular orbits. Since Raney's yaw angle (γ_R) is expressed as:

$$\gamma_R = \tan^{-1}\left(\frac{\omega/\omega_\oplus - \cos i}{\sin i \cos\beta}\right) \quad (3)$$

and considering that γ_R is the angle between the line of sight unit vector and the satellite velocity vector ($\gamma + \gamma_R = 90°$), the two steering concepts coincide for circular orbits. Therefore, the transmitting/receiving satellite has zero Doppler centroid frequency when yaw steering is performed.

Figure 3 shows the yaw angle required for this manoeuvre as a function of mean anomaly which decreases near the poles where $\underline{V}_\oplus$ is small. The yaw angles are computed separately for the two satellites.

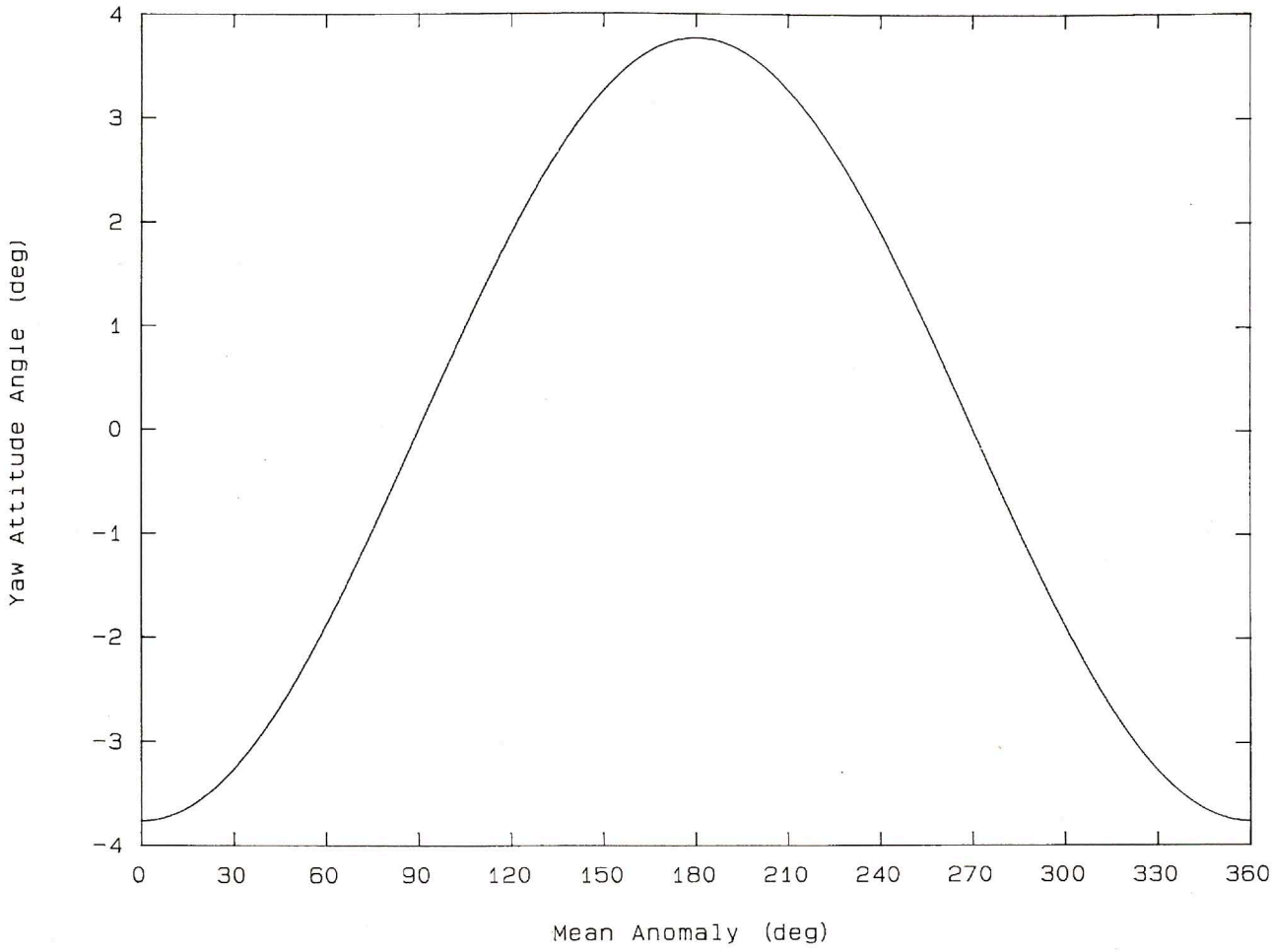

Figure 3 - Yaw attitude angle required to minimise atmospheric drag, as a function of mean anomaly.

3. DOPPLER PARAMETERS

The Doppler centroid frequency (f_D) of the transmitting/receiving satellite can be expressed as follows:

$$f_D = \frac{2}{\lambda} \frac{\dot{\underline{R}} \cdot \underline{R}}{|\underline{R}|} \tag{4}$$

where λ is the wavelength and $\underline{R}$ is the slant range computed at the centre of the beamwidth, while for the receiving-only satellite (subscript r) we get as a function of mean anomaly:

$$f_{Dr} = \frac{1}{\lambda} \left(\frac{\dot{\underline{R}} \cdot \underline{R}}{|\underline{R}|} + \frac{\dot{\underline{R}}_r \cdot \underline{R}_r}{|\underline{R}_r|} \right) \tag{5}$$

The simulated Doppler frequency without and with yaw steering are plotted in figure 4. In the first case we note a cosinusoidal curve, as shown by Li *et al.* (1985); whereas the latter curve is constant and equal to zero, as demonstrated in the previous paragraph. We wish to point out that only the frequencies of the transmitting/receiving satellite are plotted since the receiving-only satellite curves are practically similar.

The Doppler bandwidth Δf_D can be computed by eqs. (4) and (5), considering the 3dB azimuth aperture angle (dashed curve in the swath in figure 2). The simulated bandwidths are plotted in figure 5 for both satellites. When the yaw steering is not applied (B1 and B2 in figure 5), we have a cosinusoidal curve as a consequence of the variation of the Earth surface tangential velocity as a function of latitude. It is interesting to note the slight differences between the curves, due to the lag distance.

Raney (1986, 1987, 1991) thoroughly analysed the properties of orbiting SARs, so that the authors validated the simulated curves considering his analytical derivation. For circular orbit and local spherical Earth, the Doppler frequency is given by:

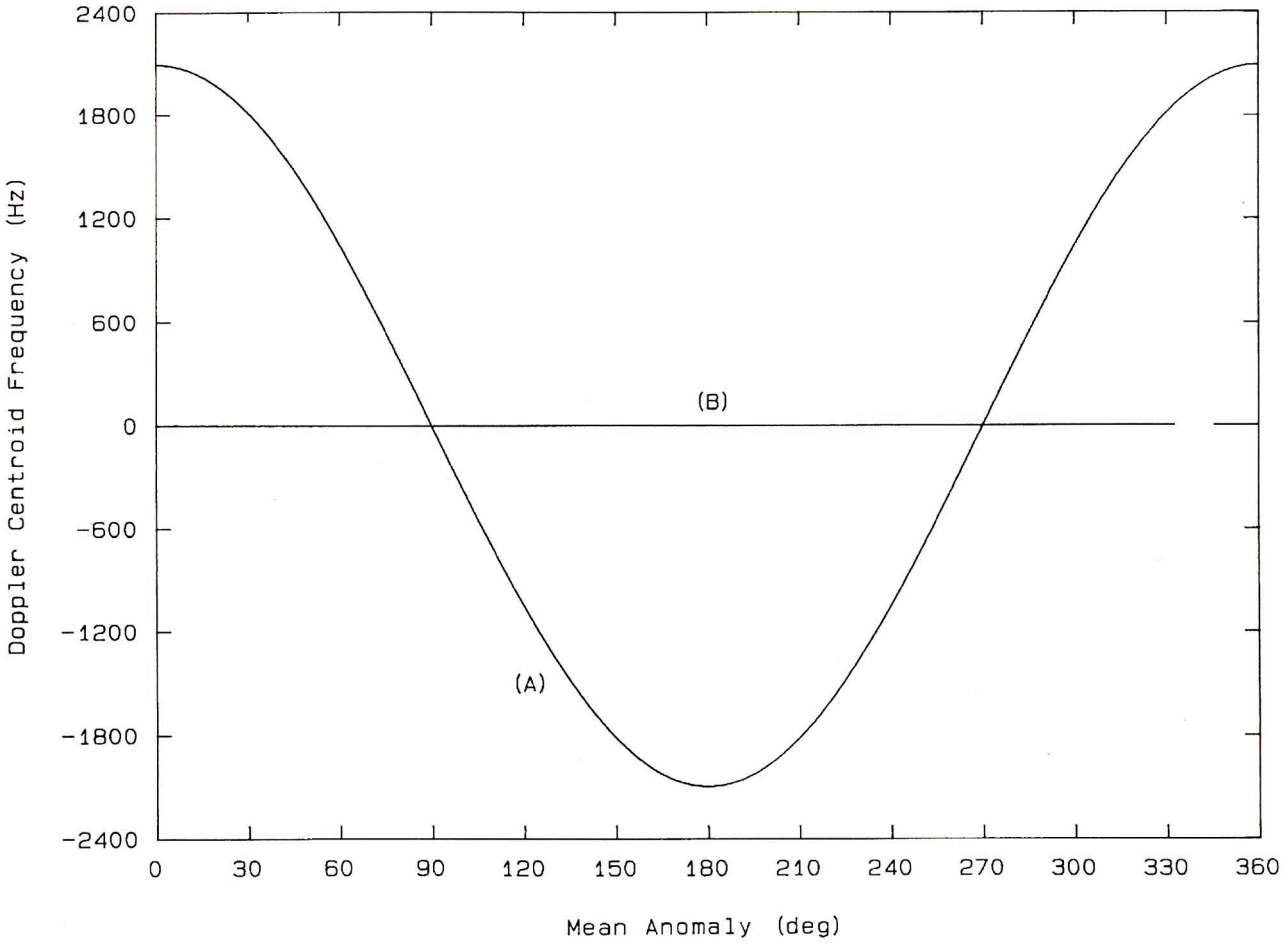

Figure 4 - Doppler frequency as a function of mean anomaly without yaw attitude angle steering (A) and with yaw steering (B).

$$f_D = \frac{2V}{\lambda} \sin\vartheta \left[\cos\gamma_R - \frac{\omega_\oplus}{\omega} \right. \quad (6)$$
$$\left. x \left(\varepsilon \cos\beta \sin i \sin\gamma_R + \cos i \cos\gamma_R \right) \right]$$

where ϑ is the off-nadir angle and ε is -1 for left looking and 1 for right looking, and the Doppler bandwidth is:

$$\Delta f_D = \frac{2V}{\lambda} \Delta\xi \left[\sin\gamma_R + \frac{\omega_\oplus}{\omega} \right. \quad (7)$$
$$\left. x \left(\varepsilon \cos\beta \sin i \cos\gamma_R - \cos i \sin\gamma_R \right) \right]$$

where $\Delta\xi$ is the 3dB azimuth angle. This bandwidth expression is derived along a constant slant range curve (solid curve in the swath in figure 2). Eq. (7) explains the constant value of bandwidth (A1 in figure 5). In fact in this case γ_R is 90° and the term depending on the mean anomaly (β) is zero. The slight differences existing in the case of receiving-only satellite (A2) are due to the variation of its position with respect to the other one and to the Earth oblateness. In particular, at the poles, where the yaw angle is zero, the A and B curves attain the same values.

It is worth noting that the assumptions of circular orbit and spherical Earth are essential for Raney's analytical derivation, whereas they are overcome by the computer simulation.

The root mean square differences between the Doppler parameters computed for the transmitting/receiving satellite and the values derived by Raney's equations (1986, 1987) are very small (Table 2).

4. ORBITAL AND INTERFEROMETRIC PARAMETERS

4.1 Swath Overlap

The two satellites are in different orbits and exhibit small differences in attitude angles due to errors and yaw stee-

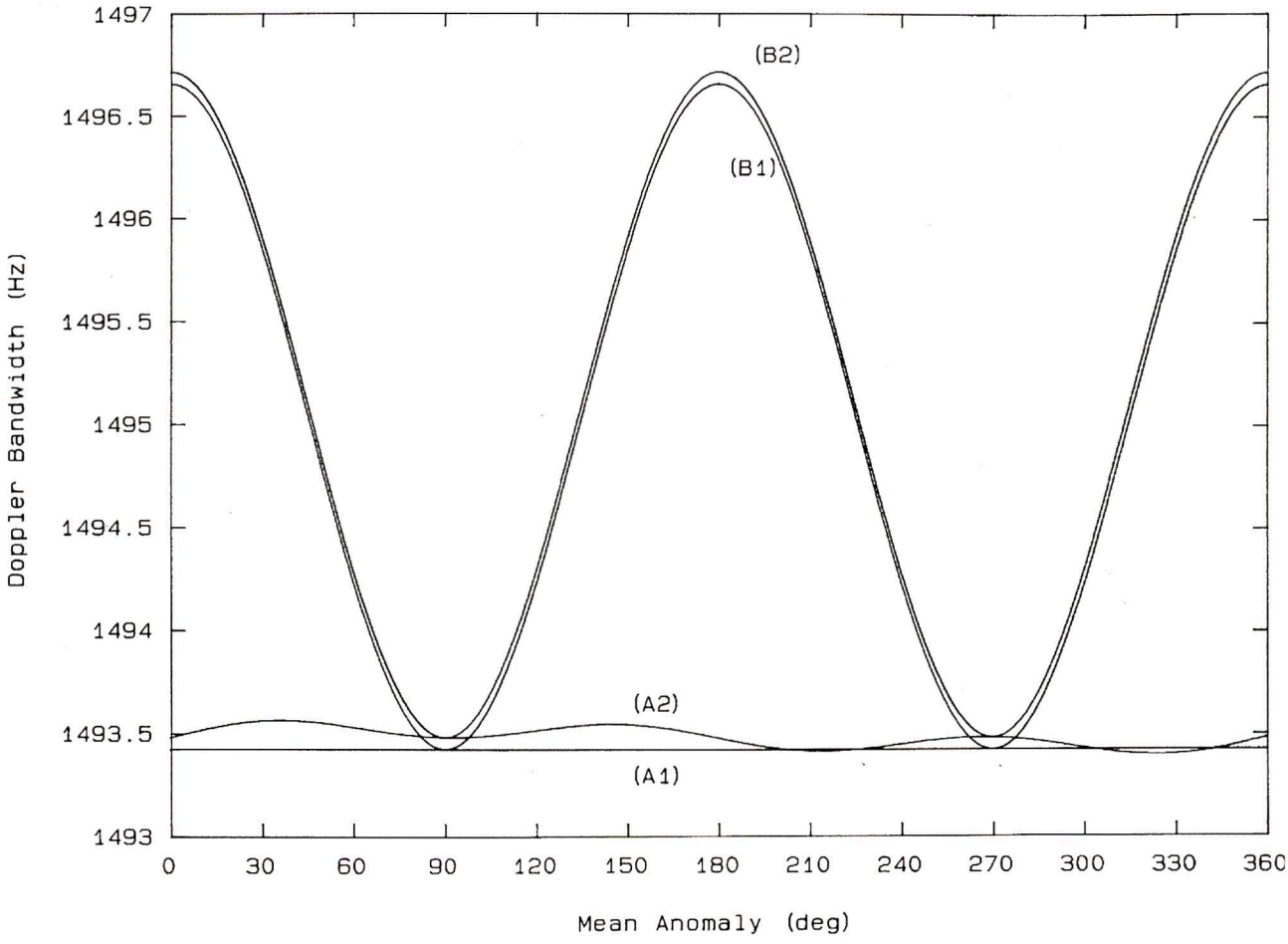

Figure 5 - Doppler bandwidth as a function of mean anomaly for the two satellites (1: transmitting/receiving satellite; 2: receiving-only satellite), without yaw attitude angle steering (A) and with yaw steering (B).

Table 2 - Root mean square differences of simulated Doppler parameters with respect to Raney's equations

Doppler Parameter	Yaw Attitude Angle Steering	RMS (Hz)
Frequency	No	$.3 \times 10^{-3}$
	Yes	0
Bandwidth	No	$.4 \times 10^{-1}$
	Yes	$.4 \times 10^{-1}$

ring. Therefore, the two radar swaths are not superimposed perfectly. Nevertheless, interferometry can be achieved only where the two satellite swaths intersect and, then, an extent of overlapping between the swaths of at least 90% must be guaranteed for interferometric coverage with satisfactory antenna gain.

To simulate this parameter an approximated geometry has been adopted. Five intersections of the antenna beam with the Earth ellipsoid have been considered for each swath: centre of beam, 3dB azimuth, 3dB range. The ten points are projected on the plane which has the minimum mean square distance from them:

$$D^2 = \frac{1}{10}\sum_{i=1}^{10}\frac{(ax_i + by_i + cz_i + d)^2}{a^2 + b^2 + c^2} \qquad (8)$$

The a, b, c, d coefficients are computed by using the Powell method for minimisation (Press *et al.*, 1992) and the x, y, z coordinates are defined with respect to an Earth-fixed right-handed reference frame (origin in the centre of the Earth, xy plane coincident with the equatorial one, xz plane containing the 0° longitude meridian). In this plane each swath is approximated by four elliptic sectors. With reference to figure 6, the range points (4 and 5) are connected by a line on which the centre of beam point (1) is projected (as point 1_i). The line perpendicular in 1_i to the ground range direction is considered, and then the azimuth

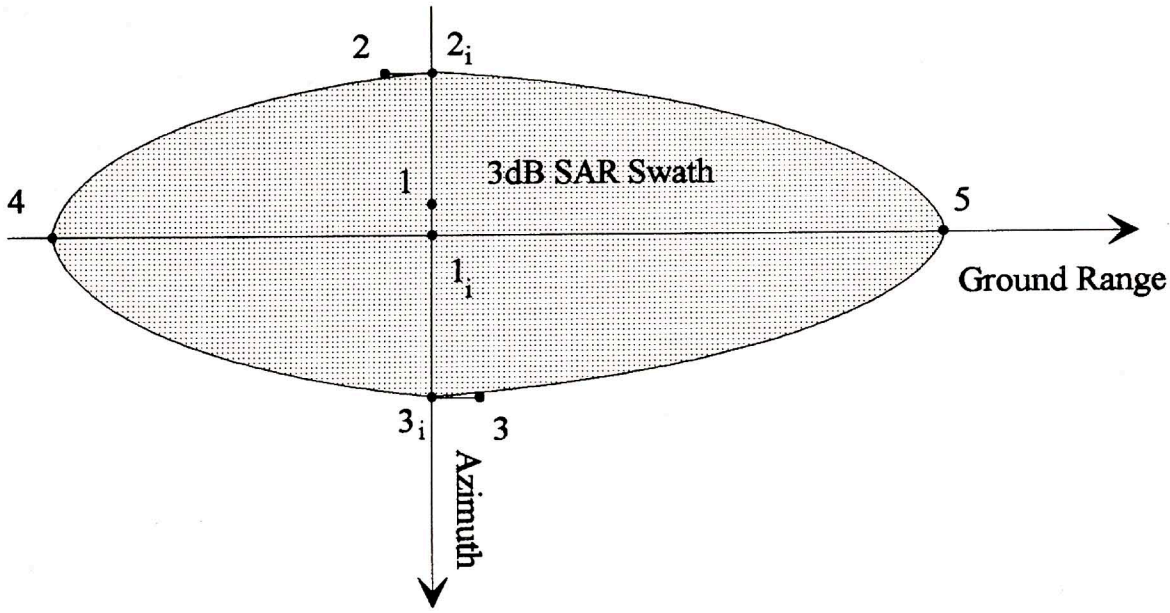

Figure 6 - Geometry for swath overlap computation. Projection in the minimum distance plane of the antenna beam interceptions with the Earth ellipsoid: centre of beam (1), 3dB azimuth (2, 3) 3dB range (4, 5).

points (2 and 3) are projected (as points 2_i and 3_i). Furthermore, the swath is approximated by the area encircled within the four elliptic sectors 42_i, 2_i5, 53_i, 3_i4. The lengths of the segments 22_i, 33_i, 11_i are calculated as a check. They are of the order of 10m, while the segments 41_i, 51_i, 3_i1_i, 2_i1_i are of the order of tens of Km. Finally, the overlap is calculated as a percentage of the area of the transmitting/receiving antenna swath.

The swath overlap without and with yaw steering is plotted in figure 7 and it is always greater than the minimum acceptable value of 90%, in both cases. The overlap increases near the poles due to the decrease of satellite distance (the component B_Y goes to zero). Moreover, the swath overlap difference between the North pole (mean anomaly 90°) and the South pole (mean anomaly 270°) depends on the Earth oblateness and on the pointing geometry. The twin satellites have a left looking angle which decreases the coverage at Northern latitudes and increases it in the Southern hemisphere. Therefore the antennae observe areas closer to the South pole than to the North pole and, of course, the Earth oblateness effect on the viewing geometry is greater in the first case.

It is worth noting that the yaw steering manoeuvre gives a positive contribution to the swath overlap, especially at the equator where the yaw angles attain their maximum and minimum values. In fact, in this case the projection of the baseline along the antenna direction decreases, that is the yaw angle contrasts the effect of B_x component. Finally, we point out that the slight discontinuities in the curves plotted in figure 7 are consequent to the approximated technique adopted to compute the overlapping areas. In fact, more accurate and time-consuming modelling can be accomplished, for instance without considering the projections on the plane but using a spherical surface. However, the proposed computation is quite effective, fast, and certainly adequate for a preliminary system study.

4.2 Baseline components

The orbits of the twin satellites are nearly parallel and their relative distance decreases from the equator to the poles. In order to attain adequate interferometric baselines in the range of latitudes ±65° (where DEMs will be derived), the distance can be neither too large (to avoid phase aliasing) nor too small (which would imply a lack of accuracy) (Li and Goldstein, 1990; Prati and Rocca, 1990; Moccia and Vetrella, 1992). Moreover, the reduced distance between the two satellites at the poles arises safety problems. Due to the above reasons, an accurate simulation of baseline components as a function of time is essential for the mission analysis.

Interferometry mainly depends on B_{y_B} which is calculated as:

$$B_{y_B} = B_x \sin\gamma + B_y \cos\gamma \qquad (9)$$

where y_B is the lateral body axis. We assume that the body reference frame axes are coincident with the satellite iner-

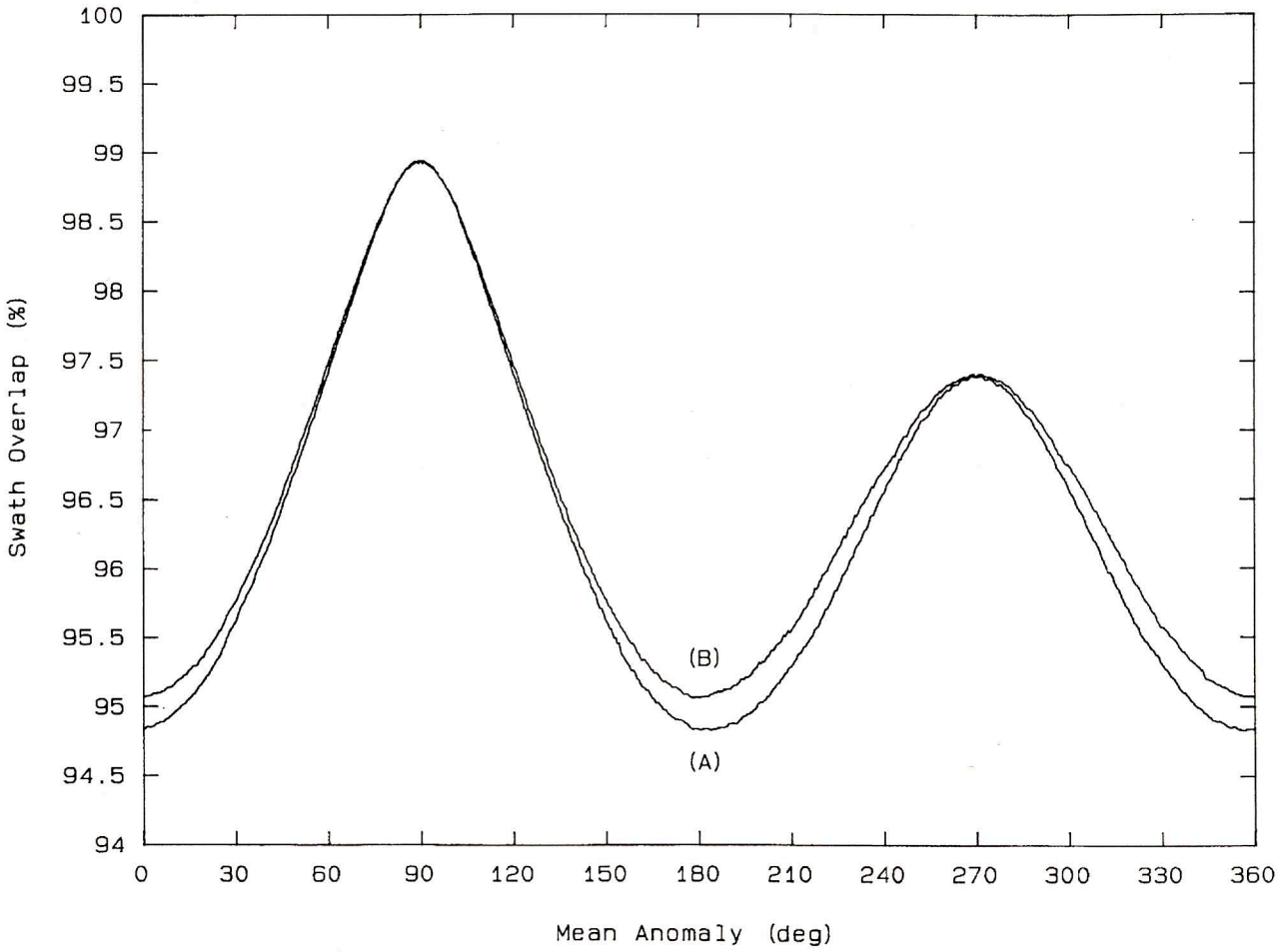

Figure 7 - Percentage swath overlap as a function of mean anomaly, without yaw attitude angle steering (A) and with yaw steering (B).

tia principal axes and that the vertical axes of the body reference frame and of the orbiting reference frame coincide. It is worth noting that B_{y_B} mainly depends on B_y, because the angle γ is small (figure 3), and that B_y decreases from the equator (mean anomaly 0° and 180°) to the poles (mean anomaly 90° and 270°), because the two orbits intersect (figure 8).

The B_x component in figure 8 is the along-track distance between the satellites and it is always satisfactory from the safety point of view. Since it is impossible to have the satellite along exactly parallel orbits, but it is correct to assume the same altitude and angular velocity for both of them, the slight periodic variations of B_x and B_z components shown in figure 8 are due to the different projections of the receiving-only satellite position with respect to the orbiting reference frame fixed to the transmitting/receiving one. In particular, at the poles, where the two satellites are closer to the line defined by the intersection of the two orbital planes, the B_z component goes to zero. Whereas the B_x component is different from the nominal value due to the angle between the two satellite velocity vectors. On the contrary, at the equator, where the two satellites approach their farthest relative distance, the B_x component attains its nominal value, whereas the B_z component increases.

4.3 Null spacing in the interferogram

The null spacing in the interferogram is an important parameter, strictly dependent on the baseline. In fact, a large spacing implies a lack of accuracy since small phase differences corresponds to large height changes, while if it is too small the fringes overlap and the phase unwrapping fails, in particular, in steep areas and/or when a low signal to noise ratio is present in the interferogram (Hirosawa and Kobayashi, 1986).

The ground range null spacing (Δx) can be computed by means of the baseline component B_{y_B}. Considering a local spherical Earth and small null angular spacing ($\Delta\vartheta$) we get:

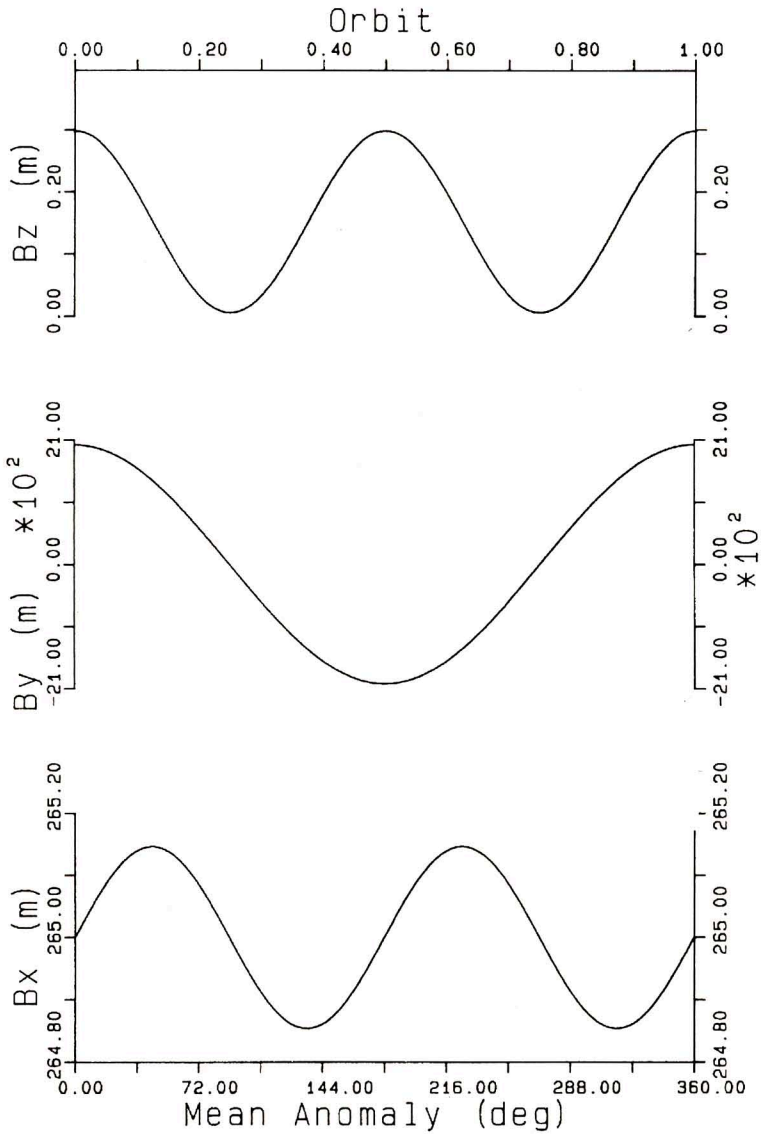

Figure 8 - Baseline components with respect to the orbiting reference frame as a function of mean anomaly.

$$\Delta x \cong \frac{\lambda R_{\oplus} R}{B_{y_B} \cos\vartheta_n (a \cos\vartheta_n - R)} \qquad (10)$$

where $R_{\oplus}$ is the local Earth radius and the subscript n refers to the null number.

The ground range null spacing is plotted in figure 9 for near and far range. Figure 9 also shows the observed point (target) latitude which has been computed at the beam centre (antenna elevation angle equal to 30° and azimuth angle equal to zero). It is worth noting that, in order enstablish a correct correspondence between latitude and null spacing, both the near and far range latitudes should have been plotted. Nevertheless, no difference would have been noted, because the three latitudes practically coincide.

The Δx curves demonstrate that interferometry is possible in the range of latitude ±65° because the null spacing varies from ~100 m (greater than three resolution elements) to ~330 m.

When $\Delta\vartheta$ is small, the slant range null spacing (ΔR) is linked to Δx by a scale factor depending on the Earth radius, the satellite altitude (h), and the null number, as follows:

$$\Delta R \cong \Delta x \left(\frac{R_{\oplus} + h}{R_{\oplus}}\right) \sin\vartheta_n \qquad (11)$$

Therefore, the slant range spacing can be easily determined by means of figure 9.

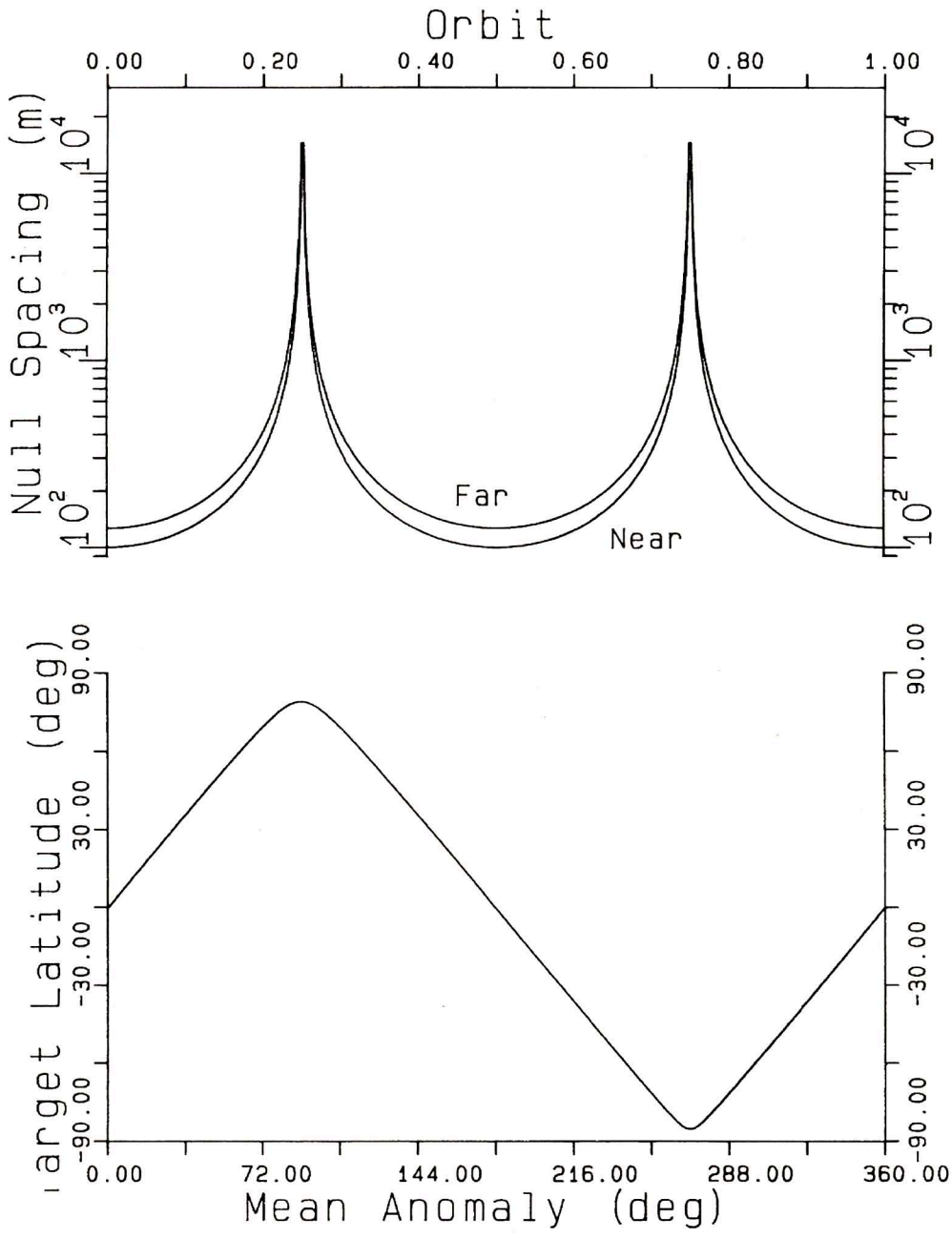

Figure 9 - Ground range null spacing (computed at near and far range) and target latitude (computed at antenna beam centre) as a function of mean anomaly.

CONCLUSIONS

This paper analysed the potentiality of the GTM with regard to the SAR interferometry application on a global scale. In particular, the study pointed out that the satellite along-track safety distance can be maintained also near the poles, provided that their relative along-track position is well designed on the node. Moreover, the interferometric baseline is adequate for the interferogram phase unwrapping and DEM generation in the range of latitudes ±65°.

With regard to the overlap between the two satellite swaths, it was shown that it is always greater than 90%, also if a yaw attitude angle steering manoeuvre is adopted to align the solar panels and the antenna along the spacecraft-atmosphere relative velocity, in order to reduce atmospheric drag. In addition, the authors demonstrated that this manoeuvre produces the zero Doppler frequency at the boresight.

The mission simulation was carried out by means of a computer code which accounts for keplerian or perturba-

ted orbit, attitude control and manoeuvres, SAR pointing geometry and radiometric characteristics, Earth ellipsoid, terrain morphology, surface backscattering characteristics, and two free flying satellites. It was validated by the computation of Doppler centroid frequency and Doppler bandwidth which were compared to analytical expressions in literature, derived under the assumption of circular orbit and local spherical Earth.

Presently, the authors are involved in the definition of the attitude requirements of the twin satellites to quantitatively study the effects of attitude errors on the swath overlap, and in the simulation of SAR interferometry on test sites where elevation maps are available to validate the GTM height measurement accuracy.

Future research activities will focus on the simulation of GTM differential interferometry by means of SAR images acquired by range steerable antennae for application in natural disasters prevention.

REFERENCES

Bate R.R., Mueller D.D. & White J.E., 1971. *Fundamentals of Astrodynamics*. Dover Publications Inc., New York, NY, 448 p.

Bertiger W.I., Lichten S.M. & Katsigris E.C., 1989. A demonstration of sub-meter GPS orbit determination and high presition user positioning. *IEEE Transactions on Aerospace and Electronic Systems*, Vol. 4, n° 2, pp. 16-25.

Bufton J.L., 1989. Laser altimetry measurements from aircraft and spacecraft. *Proceedings of the IEEE*, Vol. 77, n° 3, pp. 463-477.

D'Errico M., Moccia A. & Vetrella S., 1995. High Frequency Observation of Natural Disasters by SAR Interferometry. *Photogrammetric Engineering and Remote Sensing*, Vol. 61, n° 7, pp. 891-898.

D'Errico M., Moccia A. & Vetrella S., 1994. High Frequency Observations by GTM Antenna Range Beam Steering. *EARSeL Advances in Remote Sensing*, Vol. 3, n° 1, pp. 60-69.

Gabriel A.K. & Goldstein R.M., 1988. Crossed orbit interferometry: theory and experimental results from SIR-B. *International Journal of Remote Sensing*, Vol. 9, n° 8, pp. 857-872.

Gardner C.S., 1992. Ranging Performance of Satellite Laser Altimeters. *IEEE Transaction on Geoscience and Remote Sensing*, Vol. 30, n° 5, pp. 1061-1072.

Hagberg J.O. & Ulander L.M.H., 1993. On the Optimization of Interferometric SAR for Topographic Mapping. *IEEE Transactions on Geoscience and Remote Sensing*, Vol. 31, n° 1, pp. 303-306.

Hirosawa H. & Kobayashi N., 1986. Terrain height measurements by synthetic aperture radar with an interferometer. *International Journal of Remote Sensing*, Vol. 7, n° 3, pp. 339-348.

Joint TOPSAT NASA/ASI Working Group, 1994. Scientific requirements of a Future Space Global Topography Mission. Joint TOPSAT NASA/ASI Working Group Report, prepared for the Italian Space Agency, Rome.

Li K., Held D. N., Curlander J.C. & Wu C., 1985. Doppler Parameter Estimation for Spaceborne Synthetic Radars. *IEEE Transaction on Geoscience and Remote Sensing*, Vol. GE-23, n° 1, pp. 47-56.

Li K. & Goldstein R.M., 1990. Studies of Multibaseline Spaceborne Interferometric Synthetic Aperture Radar. *IEEE Transaction on Geoscience and Remote Sensing*, Vol. 28, n° 1, pp. 88-97.

Moccia A., Esposito S. & D'Errico M., 1994a. Height Measurements Accuracy of ERS-1 SAR Interferometry. *EARSeL Advances in Remote Sensing*, Vol. 3, n° 1, pp. 94-108.

Moccia A. & Vetrella S., 1992. A Tethered Interferometric Synthetic Aperture Radar (SAR) for a Topographic Mission. *IEEE Transactions on Geoscience and Remote Sensing*, Vol. 30, n° 1, pp. 103-109.

Moccia A., Vetrella S. & Ponte S., 1994b. Passive and Active Calibrators Characterization by Using a Spaceborne SAR System Simulator. *IEEE Transactions on Geoscience and Remote Sensing*, Vol. 32, n° 3, pp 715-721.

Prati C. & Rocca F., 1990. Limits to the resolution of elevation maps from stereo SAR images. International Journal of Remote Sensing, Vol. 11, No. 12, pp. 2215-2235.

Prati C., Rocca F. & Monti Guarnieri A., 1992. SAR Interferometry experiments with ERS-1. Proc. First ERS-1 Symposium, ESA SP-359, pp. 211-218.

Press W.H., Teukolsky S.A., Vetterling W.T. & Flannery B.P., 1992. Numerical Recipes: The Art of Scientific Computing (2nd Edition), Cambridge University Press, Cambridge, MA, USA, pp. 963.

Raney R.K., 1986. Doppler properties of radars in circular orbits. *International Journal of Remote Sensing*, Vol. 7, n° 9, pp. 1153-1162.

Raney R.K., 1987. A Comment on Doppler FM Rate. *International Journal of Remote Sensing*, Vol. 8, n° 7, pp. 1091-1092.

Raney R.K., 1991. Considerations for SAR Image Quantification Unique to Orbital Systems. *IEEE Transactions on Geoscience and Remote Sensing*, Vol. 29, n° 5, pp 754-760.

Rodriguez E. & Martin J.M., 1992. Theory and design of interferometric synthetic aperture radars. *IEE Proceedings-F*, Vol. 2, pp. 147-159.

Salazar R.P. & Kakuda R.Y., 1994. The Global Topography Mission (TOPSAT). *EARSeL Advances in Remote Sensing*, Vol. 3, n° 1, pp 109-116.

Topographic Science Working Group, 1988. Topographic Science Working Group Report to the Land Processing Branch, Earth Science and Application Division, NASA Headquarters. Lunar and Planetary Institute, Houston, pp. 64.

Yunck T.P., Melbourne W.G. & Thornton C.L., 1985. GPS-Based Satellite Tracking System for Precise Positioning. *IEEE Transactions on Geoscience and Remote Sensing*, Vol. GE-23, n° 4, pp. 450-457.

Zebker H.A. & Villasenor J., 1992. Decorrelation in Interferometric Radar Echos. *IEEE Transactions on Geoscience and Remote Sensing*, Vol. 30, n° 5, pp. 950-959.

Zebker H.A., Werner C.L., Rosen P.A. & Hensley S., 1994. Accuracy of topographic maps perived from ERS-1 interferometric radar. *IEEE Transactions on Geoscience and Remote Sensing*, Vol. 32, n° 4, pp. 823-836.